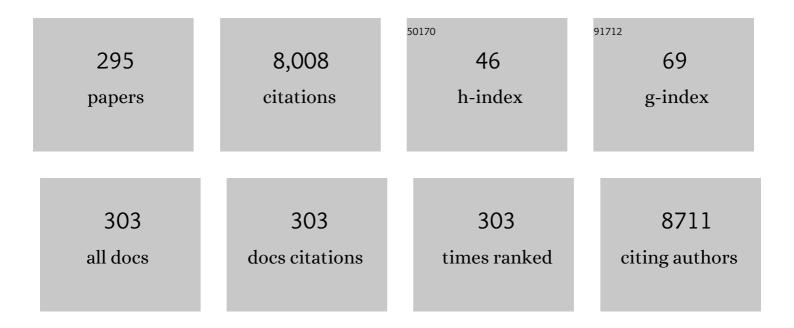
Jan S Kirschke

List of Publications by Year in descending order

Source: https://exaly.com/author-pdf/6011759/publications.pdf Version: 2024-02-01



#	Article	IF	CITATIONS
1	ISLES 2015 - A public evaluation benchmark for ischemic stroke lesion segmentation from multispectral MRI. Medical Image Analysis, 2017, 35, 250-269.	7.0	360
2	Five Freely Circulating miRNAs and Bone Tissue miRNAs Are Associated With Osteoporotic Fractures. Journal of Bone and Mineral Research, 2014, 29, 1718-1728.	3.1	292
3	Cartilage and meniscal T2 relaxation time as non-invasive biomarker for knee osteoarthritis and cartilage repair procedures. Osteoarthritis and Cartilage, 2013, 21, 1474-1484.	0.6	159
4	Inter-subject comparison of MRI knee cartilage thickness. Medical Image Analysis, 2008, 12, 120-135.	7.0	127
5	Advances in osteoporosis imaging. European Journal of Radiology, 2009, 71, 440-449.	1.2	127
6	Bone marrow fat quantification in the presence of trabecular bone: Initial comparison between waterâ€fat imaging and singleâ€voxel MRS. Magnetic Resonance in Medicine, 2014, 71, 1158-1165.	1.9	127
7	Risk of cement leakage and pulmonary embolism by bone cement-augmented pedicle screw fixation of the thoracolumbar spine. Spine Journal, 2017, 17, 837-844.	0.6	116
8	VerSe: A Vertebrae labelling and segmentation benchmark for multi-detector CT images. Medical Image Analysis, 2021, 73, 102166.	7.0	112
9	Cortical pathology in multiple sclerosis detected by the <scp>T</scp> 1/ <scp>T</scp> 2â€weighted ratio from routine magnetic resonance imaging. Annals of Neurology, 2017, 82, 519-529.	2.8	102
10	Trabecular Bone Structure of the Calcaneus: Comparison of MR Imaging at 3.0 and 1.5 T with Micro-CT as the Standard of Reference. Radiology, 2006, 239, 488-496.	3.6	101
11	Improved prediction of incident vertebral fractures using opportunistic QCT compared to DXA. European Radiology, 2019, 29, 4980-4989.	2.3	99
12	miRNAs in bone tissue correlate to bone mineral density and circulating miRNAs are gender independent in osteoporotic patients. Scientific Reports, 2017, 7, 15861.	1.6	96
13	Volumetric Quantitative CT of the Spine and Hip Derived from Contrast-Enhanced MDCT: Conversion Factors. American Journal of Roentgenology, 2007, 188, 1294-1301.	1.0	95
14	Radiolucent Carbon Fiber–Reinforced Pedicle Screws for Treatment of Spinal Tumors: Advantages for Radiation Planning and Follow-Up Imaging. World Neurosurgery, 2017, 105, 294-301.	0.7	93
15	In Vitro and in Vivo Spiral CT to Determine Bone Mineral Density: Initial Experience in Patients at Risk for Osteoporosis. Radiology, 2004, 231, 805-811.	3.6	87
16	MR imaging of the ankle at 3 Tesla and 1.5 Tesla: protocol optimization and application to cartilage, ligament and tendon pathology in cadaver specimens. European Radiology, 2007, 17, 1518-1528.	2.3	87
17	DeepVesselNet: Vessel Segmentation, Centerline Prediction, and Bifurcation Detection in 3-D Angiographic Volumes. Frontiers in Neuroscience, 2020, 14, 592352.	1.4	83
18	Structural Analysis of Trabecular Bone of the Proximal Femur Using Multislice Computed Tomography: A Comparison with Dual X-Ray Absorptiometry for Predicting Biomechanical Strength In Vitro. Calcified Tissue International, 2006, 78, 78-89.	1.5	82

#	Article	IF	CITATIONS
19	Assessment of whole spine vertebral bone marrow fat using chemical shiftâ€encoding based waterâ€fat MRI. Journal of Magnetic Resonance Imaging, 2015, 42, 1018-1023.	1.9	82
20	Revision Rate of Misplaced Pedicle Screws of the Thoracolumbar Spine–Comparison of Three-Dimensional Fluoroscopy Navigation with Freehand Placement: A Systematic Analysis and Review of the Literature. World Neurosurgery, 2018, 109, e24-e32.	0.7	82
21	Bone Mineral Density Values Derived from Routine Lumbar Spine Multidetector Row CT Predict Osteoporotic Vertebral Fractures and Screw Loosening. American Journal of Neuroradiology, 2014, 35, 1628-1633.	1.2	74
22	Opportunistic osteoporosis screening in multi-detector CT images via local classification of textures. Osteoporosis International, 2019, 30, 1275-1285.	1.3	72
23	A Vertebral Segmentation Dataset with Fracture Grading. Radiology: Artificial Intelligence, 2020, 2, e190138.	3.0	71
24	MR-Based Assessment of Bone Marrow Fat in Osteoporosis, Diabetes, and Obesity. Frontiers in Endocrinology, 2016, 7, 74.	1.5	70
25	MR-based assessment of body fat distribution and characteristics. European Journal of Radiology, 2016, 85, 1512-1518.	1.2	68
26	X-ray-based quantitative osteoporosis imaging at the spine. Osteoporosis International, 2020, 31, 233-250.	1.3	68
27	Association of paraspinal muscle water–fat MRI-based measurements with isometric strength measurements. European Radiology, 2019, 29, 599-608.	2.3	66
28	Detection of osteoporotic vertebral fractures using multidetector CT. Osteoporosis International, 2006, 17, 608-615.	1.3	65
29	Anatomical Variation of Age-Related Changes in Vertebral Bone Marrow Composition Using Chemical Shift Encoding-Based Water–Fat Magnetic Resonance Imaging. Frontiers in Endocrinology, 2018, 9, 141.	1.5	65
30	<scp>MRI</scp> â€Based Quantitative Osteoporosis Imaging at the Spine and Femur. Journal of Magnetic Resonance Imaging, 2021, 54, 12-35.	1.9	61
31	Significance of sagittal reformations in routine thoracic and abdominal multislice CT studies for detecting osteoporotic fractures and other spine abnormalities. European Radiology, 2008, 18, 1696-1702.	2.3	60
32	Associations between clinical outcome and navigated transcranial magnetic stimulation characteristics in patients with motor-eloquent brain lesions: a combined navigated transcranial magnetic stimulation–diffusion tensor imaging fiber tracking approach. Journal of Neurosurgery, 2018, 128, 800-810.	0.9	60
33	Automated segmentation of changes in FLAIR-hyperintense white matter lesions in multiple sclerosis on serial magnetic resonance imaging. NeuroImage: Clinical, 2019, 23, 101849.	1.4	60
34	Diffusion tensor image features predict IDH genotype in newly diagnosed WHO grade II/III gliomas. Scientific Reports, 2017, 7, 13396.	1.6	57
35	BMD measurements of the spine derived from sagittal reformations of contrast-enhanced MDCT without dedicated software. European Journal of Radiology, 2011, 80, e140-e145.	1.2	55
36	Bisphosphonate and Medication-Related Osteonecrosis of the Jaw: A Review. Seminars in Musculoskeletal Radiology, 2016, 20, 305-314.	0.4	54

#	Article	IF	CITATIONS
37	Converted Lumbar BMD Values Derived from Sagittal Reformations of Contrast-Enhanced MDCT Predict Incidental Osteoporotic Vertebral Fractures. Calcified Tissue International, 2012, 90, 481-487.	1.5	53
38	Volume versus surface-based cortical thickness measurements: A comparative study with healthy controls and multiple sclerosis patients. PLoS ONE, 2017, 12, e0179590.	1.1	53
39	Trabecular Bone Structure of the Distal Radius, the Calcaneus, and the Spine. Investigative Radiology, 2004, 39, 487-497.	3.5	52
40	The need for <i>T</i> ₂ correction on MRS-based vertebral bone marrow fat quantification: implications for bone marrow fat fraction age dependence. NMR in Biomedicine, 2015, 28, 432-439.	1.6	52
41	MRâ€detected changes in liver fat, abdominal fat, and vertebral bone marrow fat after a fourâ€week calorie restriction in obese women. Journal of Magnetic Resonance Imaging, 2015, 42, 1272-1280.	1.9	51
42	Combined Image Processing Techniques for Characterization of MRI Cartilage of the Knee. , 2005, 2005, 3043-6.		50
43	BraTS Toolkit: Translating BraTS Brain Tumor Segmentation Algorithms Into Clinical and Scientific Practice. Frontiers in Neuroscience, 2020, 14, 125.	1.4	50
44	Automatic opportunistic osteoporosis screening in routine CT: improved prediction of patients with prevalent vertebral fractures compared to DXA. European Radiology, 2021, 31, 6069-6077.	2.3	50
45	T2 assessment and clinical outcome following autologous matrix-assisted chondrocyte and osteochondral autograft transplantation. Osteoarthritis and Cartilage, 2009, 17, 1576-1582.	0.6	49
46	Relaxation effects of ferucarbotranâ€labeled mesenchymal stem cells at 1.5T and 3T: Discrimination of viable from lysed cells. Magnetic Resonance in Medicine, 2009, 62, 325-332.	1.9	48
47	Sonographic assessment of abdominal fat distribution during the first year of infancy. Pediatric Research, 2015, 78, 342-350.	1.1	48
48	Retrospective Analysis of Radiological Recurrence Patterns in Glioblastoma, Their Prognostic Value And Association to Postoperative Infarct Volume. Scientific Reports, 2018, 8, 4561.	1.6	48
49	Cell labeling with the positive MR contrast agent Gadofluorine M. European Radiology, 2007, 17, 1226-1234.	2.3	47
50	Magnetic Resonance Imaging of the Ankle at 3.0 Tesla and 1.5 Tesla in Human Cadaver Specimens With Artificially Created Lesions of Cartilage and Ligaments. Investigative Radiology, 2008, 43, 604-611.	3.5	47
51	Is multidetector CT-based bone mineral density and quantitative bone microstructure assessment at the spine still feasible using ultra-low tube current and sparse sampling?. European Radiology, 2017, 27, 5261-5271.	2.3	47
52	Analysis of Trabecular Bone Structure with Multidetector Spiral Computed Tomography in a Simulated Soft-Tissue Environment. Calcified Tissue International, 2007, 80, 366-373.	1.5	46
53	Cartilage Repair Surgery: Outcome Evaluation by Using Noninvasive Cartilage Biomarkers Based on Quantitative MRI Techniques?. BioMed Research International, 2014, 2014, 1-17.	0.9	46
54	Modeling of <i>T</i> ₂ * decay in vertebral bone marrow fat quantification. NMR in Biomedicine, 2015, 28, 1535-1542.	1.6	46

#	Article	IF	CITATIONS
55	Bone mineral density measurements derived from dual-layer spectral CT enable opportunistic screening for osteoporosis. European Radiology, 2019, 29, 6355-6363.	2.3	46
56	Accuracy of Unenhanced MRI in the Detection of New Brain Lesions in Multiple Sclerosis. Radiology, 2019, 291, 429-435.	3.6	46
57	Proximal Femur Specimens: Automated 3D Trabecular Bone Mineral Density Analysis at Multidetector CT—Correlation with Biomechanical Strength Measurement. Radiology, 2008, 247, 472-481.	3.6	45
58	MR arthrography including abduction and external rotation images in the assessment of atraumatic multidirectional instability of the shoulder. European Radiology, 2014, 24, 1376-1385.	2.3	42
59	Language pathway tracking: comparing nTMS-based DTI fiber tracking with a cubic ROIs-based protocol. Journal of Neurosurgery, 2017, 126, 1006-1014.	0.9	42
60	Associations Between Lumbar Vertebral Bone Marrow and Paraspinal Muscle Fat Compositions—An Investigation by Chemical Shift Encoding-Based Water-Fat MRI. Frontiers in Endocrinology, 2018, 9, 563.	1.5	39
61	Diagnostic Value of CT Arthrography for Evaluation of Osteochondral Lesions at the Ankle. BioMed Research International, 2016, 2016, 1-11.	0.9	38
62	Visualization of subcortical language pathways by diffusion tensor imaging fiber tracking based on rTMS language mapping. Brain Imaging and Behavior, 2017, 11, 899-914.	1.1	38
63	Robust and parallel scalable iterative solutions for large-scale finite cell analyses. Finite Elements in Analysis and Design, 2019, 163, 14-30.	1.7	37
64	Btrfly Net: Vertebrae Labelling with Energy-Based Adversarial Learning of Local Spine Prior. Lecture Notes in Computer Science, 2018, , 649-657.	1.0	37
65	Fast High-Spatial-Resolution MRI of the Ankle with Parallel Imaging Using GRAPPA at 3 T. American Journal of Roentgenology, 2007, 189, 240-245.	1.0	36
66	Prediction of bone strength by μCT and MDCT-based finite-element-models: How much spatial resolution is needed?. European Journal of Radiology, 2014, 83, e36-e42.	1.2	36
67	Association of MRS-Based Vertebral Bone Marrow Fat Fraction with Bone Strength in a Human In Vitro Model. Journal of Osteoporosis, 2015, 2015, 1-8.	0.1	36
68	Feasibility of nTMS-based DTI fiber tracking of language pathways in neurosurgical patients using a fractional anisotropy threshold. Journal of Neuroscience Methods, 2016, 267, 45-54.	1.3	36
69	Fatigue in multiple sclerosis: Associations with clinical, MRI and CSF parameters. Multiple Sclerosis Journal, 2018, 24, 1115-1125.	1.4	36
70	DiamondGAN: Unified Multi-modal Generative Adversarial Networks for MRI Sequences Synthesis. Lecture Notes in Computer Science, 2019, , 795-803.	1.0	36
71	CT-like images based on T1 spoiled gradient-echo and ultra-short echo time MRI sequences for the assessment of vertebral fractures and degenerative bone changes of the spine. European Radiology, 2021, 31, 4680-4689.	2.3	35
72	Volumetric Cartilage Measurements of Porcine Knee at 1.5-T and 3.0-T MR Imaging: Evaluation of Precision and Accuracy. Radiology, 2006, 241, 399-406.	3.6	34

#	Article	IF	CITATIONS
73	Double Inversion Recovery Sequence of the Cervical Spinal Cord in Multiple Sclerosis and Related Inflammatory Diseases. American Journal of Neuroradiology, 2015, 36, 219-225.	1.2	34
74	Prognostic Value of O-(2-[18F]-Fluoroethyl)-L-Tyrosine-Positron Emission Tomography Imaging for Histopathologic Characteristics and Progression-Free Survival in Patients with Low-Grade Glioma. World Neurosurgery, 2016, 89, 230-239.	0.7	34
75	MR and CT Imaging to Optimize CT-Guided Biopsies in Suspected Spondylodiscitis. World Neurosurgery, 2017, 99, 726-734.e7.	0.7	34
76	Phaseâ€field boundary conditions for the voxel finite cell method: Surfaceâ€free stress analysis of CTâ€based bone structures. International Journal for Numerical Methods in Biomedical Engineering, 2017, 33, e2880.	1.0	33
77	Local Fractional Anisotropy Is Reduced in Areas with Tumor Recurrence in Glioblastoma. Radiology, 2017, 283, 499-507.	3.6	33
78	Prognostic Value of Tumor Volume in Glioblastoma Patients: Size Also Matters for Patients with Incomplete Resection. Annals of Surgical Oncology, 2018, 25, 558-564.	0.7	33
79	A large, curated, open-source stroke neuroimaging dataset to improve lesion segmentation algorithms. Scientific Data, 2022, 9, .	2.4	33
80	Association of Quadriceps Muscle Fat With Isometric Strength Measurements in Healthy Males Using Chemical Shift Encoding-Based Water-Fat Magnetic Resonance Imaging. Journal of Computer Assisted Tomography, 2016, 40, 447-451.	0.5	32
81	Bone mineral density measurements in vertebral specimens and phantoms using dual-layer spectral computed tomography. Scientific Reports, 2017, 7, 17519.	1.6	32
82	Automatic detection of osteoporotic vertebral fractures in routine thoracic and abdominal MDCT. European Radiology, 2014, 24, 872-880.	2.3	31
83	In-Vivo Assessment of Femoral Bone Strength Using Finite Element Analysis (FEA) Based on Routine MDCT Imaging: A Preliminary Study on Patients with Vertebral Fractures. PLoS ONE, 2015, 10, e0116907.	1.1	31
84	Texture analysis of vertebral bone marrow using chemical shift encoding–based water-fat MRI: a feasibility study. Osteoporosis International, 2019, 30, 1265-1274.	1.3	30
85	Correlation of X-Ray Vector Radiography to Bone Micro-Architecture. Scientific Reports, 2014, 4, 3695.	1.6	29
86	Improving bone strength prediction in human proximal femur specimens through geometrical characterization of trabecular bone microarchitecture and support vector regression. Journal of Electronic Imaging, 2014, 23, 013013.	0.5	28
87	View-Angle Tilting and Slice-Encoding Metal Artifact Correction for Artifact Reduction in MRI: Experimental Sequence Optimization for Orthopaedic Tumor Endoprostheses and Clinical Application. PLoS ONE, 2015, 10, e0124922.	1.1	28
88	Patterns and Time Dependence of Unspecific Enhancement in Postoperative Magnetic Resonance Imaging After Glioblastoma Resection. World Neurosurgery, 2016, 90, 440-447.	0.7	28
89	Analysis of fractional anisotropy facilitates differentiation of glioblastoma and brain metastases in a clinical setting. European Journal of Radiology, 2016, 85, 2182-2187.	1.2	28
90	Multiâ€level <i>hp</i> â€finite cell method for embedded interface problems with application in biomechanics. International Journal for Numerical Methods in Biomedical Engineering, 2018, 34, e2951.	1.0	28

#	Article	IF	CITATIONS
91	Acceleration of Double Inversion Recovery Sequences in Multiple Sclerosis With Compressed Sensing. Investigative Radiology, 2019, 54, 319-324.	3.5	28
92	Feasibility of opportunistic osteoporosis screening in routine contrast-enhanced multi detector computed tomography (MDCT) using texture analysis. Osteoporosis International, 2018, 29, 825-835.	1.3	27
93	Associations of thigh muscle fat infiltration with isometric strength measurements based on chemical shift encoding-based water-fat magnetic resonance imaging. European Radiology Experimental, 2019, 3, 45.	1.7	27
94	Trabecular Bone Structure Obtained From Multislice Spiral Computed Tomography of the Calcaneus Predicts Osteoporotic Vertebral Deformities. Journal of Computer Assisted Tomography, 2005, 29, 246-253.	0.5	26
95	Imaging Characteristics of DHOG, a Hepatobiliary Contrast Agent for Preclinical MicroCT in Mice. Academic Radiology, 2008, 15, 342-349.	1.3	26
96	Trabecular bone structure analysis of the spine using clinical MDCT: can it predict vertebral bone strength?. Journal of Bone and Mineral Metabolism, 2014, 32, 56-64.	1.3	26
97	Labeling Vertebrae with Two-dimensional Reformations of Multidetector CT Images: An Adversarial Approach for Incorporating Prior Knowledge of Spine Anatomy. Radiology: Artificial Intelligence, 2020, 2, e190074.	3.0	26
98	Takayasu's arteritis in pregnancy: review of literature and discussion. Journal of Perinatal Medicine, 2010, 38, 55-62.	0.6	25
99	Preoperative language mapping by repetitive navigated transcranial magnetic stimulation and diffusion tensor imaging fiber tracking and their comparison to intraoperative stimulation. Neuroradiology, 2016, 58, 807-818.	1.1	25
100	Magnetic resonance imaging of the inferior alveolar nerve with special regard to metal artifact reduction. Journal of Cranio-Maxillo-Facial Surgery, 2017, 45, 558-569.	0.7	25
101	Accuracy of CT-navigated pedicle screw positioning in the cervical and upper thoracic region with and without prior anterior surgery and ventral plating. Bone and Joint Journal, 2017, 99-B, 1373-1380.	1.9	25
102	Improved Brachial Plexus Visualization Using an Adiabatic iMSDE-Prepared STIR 3D TSE. Clinical Neuroradiology, 2019, 29, 631-638.	1.0	25
103	Vertebral Artery Patency and Thrombectomy in Basilar Artery Occlusions. Stroke, 2019, 50, 389-395.	1.0	25
104	Bone mineral density measurements of the proximal femur from routine contrast-enhanced MDCT data sets correlate with dual-energy X-ray absorptiometry. European Radiology, 2013, 23, 505-512.	2.3	24
105	Coherent Superposition in Grating-Based Directional Dark-Field Imaging. PLoS ONE, 2013, 8, e61268.	1.1	24
106	Multidetector Computed Tomography Imaging. Journal of Computer Assisted Tomography, 2018, 42, 441-447.	0.5	24
107	Bilateral cartilage T2 mapping 9 years after Mega-OATS implantation at the knee: a quantitative 3T MRI study. Osteoarthritis and Cartilage, 2015, 23, 2119-2128.	0.6	23
108	Infarct volume after glioblastoma surgery as an independent prognostic factor. Oncotarget, 2016, 7, 61945-61954.	0.8	23

#	Article	IF	CITATIONS
109	Cognitive impairment in early MS: contribution of white matter lesions, deep grey matter atrophy, and cortical atrophy. Journal of Neurology, 2020, 267, 2307-2318.	1.8	23
110	Mapping of cerebral metabolic rate of oxygen using dynamic susceptibility contrast and blood oxygen level dependent MR imaging in acute ischemic stroke. Neuroradiology, 2015, 57, 1253-1261.	1.1	22
111	Distinguishing Benign and Malignant Vertebral Fractures Using CT and MRI. Seminars in Musculoskeletal Radiology, 2016, 20, 345-352.	0.4	22
112	Two patients with G <i>MPPB</i> mutation: The overlapping phenotypes of limb-girdle myasthenic syndrome and limb-girdle muscular dystrophy dystroglycanopathy. Muscle and Nerve, 2017, 56, 334-340.	1.0	22
113	Loss of Subcortical Language Pathways Correlates with Surgery-Related Aphasia in Patients with Brain Tumor: An Investigation via Repetitive Navigated Transcranial Magnetic Stimulation–Based Diffusion Tensor Imaging Fiber Tracking. World Neurosurgery, 2018, 111, e806-e818.	0.7	22
114	Adjuvant stereotactic fractionated radiotherapy to the resection cavity in recurrent glioblastoma – the GlioCave study (NOA 17 – ARO 2016/3 – DKTK ROG trial). BMC Cancer, 2018, 18, 15.	1.1	22
115	Thigh muscle segmentation of chemical shift encoding-based water-fat magnetic resonance images: The reference database MyoSegmenTUM. PLoS ONE, 2018, 13, e0198200.	1.1	22
116	Retrospective distortion correction of diffusion tensor imaging data by semi-elastic image fusion – Evaluation by means of anatomical landmarks. Clinical Neurology and Neurosurgery, 2019, 183, 105387.	0.6	22
117	Paraspinal Muscle DTI Metrics Predict Muscle Strength. Journal of Magnetic Resonance Imaging, 2019, 50, 816-823.	1.9	22
118	Magnetic Resonance Imaging of the Brain Using Compressed Sensing– Quality Assessment in Daily Clinical Routine. Clinical Neuroradiology, 2020, 30, 279-286.	1.0	22
119	Effect of the intervertebral disc on vertebral bone strength prediction: a finite-element study. Spine Journal, 2020, 20, 665-671.	0.6	22
120	A computed tomography vertebral segmentation dataset with anatomical variations and multi-vendor scanner data. Scientific Data, 2021, 8, 284.	2.4	22
121	Imaging of Trabecular Bone Structure. Seminars in Musculoskeletal Radiology, 2002, 06, 253-262.	0.4	21
122	Balloon osteoplasty—a new technique for reduction and stabilisation of impression fractures in the tibial plateau: A cadaver study and first clinical application. International Orthopaedics, 2012, 36, 1937-1940.	0.9	21
123	Osteoporosis Is the Most Important Risk Factor for Odontoid Fractures in the Elderly. Journal of Bone and Mineral Research, 2017, 32, 1582-1588.	3.1	21
124	Gender- and Age-Related Changes in Trunk Muscle Composition Using Chemical Shift Encoding-Based Water–Fat MRI. Nutrients, 2018, 10, 1972.	1.7	21
125	Three-material decomposition with dual-layer spectral CT compared to MRI for the detection of bone marrow edema in patients with acute vertebral fractures. Skeletal Radiology, 2018, 47, 1533-1540.	1.2	21
126	Multi-detector CT imaging: impact of virtual tube current reduction and sparse sampling on detection of vertebral fractures. European Radiology, 2019, 29, 3606-3616.	2.3	21

#	Article	IF	CITATIONS
127	Opportunistic Osteoporosis Screening Reveals Low Bone Density in Patients With Screw Loosening After Lumbar Semi-Rigid Instrumentation: A Case-Control Study. Frontiers in Endocrinology, 2020, 11, 552719.	1.5	21
128	Attention-Driven Deep Learning for Pathological Spine Segmentation. Lecture Notes in Computer Science, 2018, , 108-119.	1.0	21
129	Accelerated stem cell labeling with ferucarbotran and protamine. European Radiology, 2010, 20, 640-648.	2.3	20
130	Cortical and trabecular bone structure analysis at the distal radius—prediction of biomechanical strength by DXA and MRI. Journal of Bone and Mineral Metabolism, 2013, 31, 212-221.	1.3	20
131	Effects of dose reduction on bone strength prediction using finite element analysis. Scientific Reports, 2016, 6, 38441.	1.6	20
132	Interhemispheric connectivity revealed by diffusion tensor imaging fiber tracking derived from navigated transcranial magnetic stimulation maps as a sign of language function at risk in patients with brain tumors. Journal of Neurosurgery, 2017, 126, 222-233.	0.9	20
133	Decreased water T ₂ in fatty infiltrated skeletal muscles of patients with neuromuscular diseases. NMR in Biomedicine, 2019, 32, e4111.	1.6	20
134	Highly accelerated time-of-flight magnetic resonance angiography using spiral imaging improves conspicuity of intracranial arterial branches while reducing scan time. European Radiology, 2020, 30, 855-865.	2.3	20
135	Regional analysis of age-related local bone loss in the spine of a healthy population using 3D voxel-based modeling. Bone, 2017, 103, 233-240.	1.4	19
136	Fully automated analysis combining [18F]-FET-PET and multiparametric MRI including DSC perfusion and APTw imaging: a promising tool for objective evaluation of glioma progression. European Journal of Nuclear Medicine and Molecular Imaging, 2021, 48, 4445-4455.	3.3	19
137	Safe Brain Tumor Resection Does not Depend on Surgery Alone - Role of Hemodynamics. Scientific Reports, 2017, 7, 5585.	1.6	18
138	DXA-equivalent quantification of bone mineral density using dual-layer spectral CT scout scans. European Radiology, 2019, 29, 4624-4634.	2.3	18
139	Simulation Training in Neuroangiography—Validation and Effectiveness. Clinical Neuroradiology, 2021, 31, 465-473.	1.0	18
140	MR-based proton density fat fraction (PDFF) of the vertebral bone marrow differentiates between patients with and without osteoporotic vertebral fractures. Osteoporosis International, 2022, 33, 487-496.	1.3	18
141	B1-insensitive T2 mapping of healthy thigh muscles using a T2-prepared 3D TSE sequence. PLoS ONE, 2017, 12, e0171337.	1.1	18
142	Advances of 3T MR imaging in visualizing trabecular bone structure of the calcaneus are partially SNRâ€independent: Analysis using simulated noise in relation to microâ€CT, 1.5T MRI, and biomechanical strength. Journal of Magnetic Resonance Imaging, 2009, 29, 132-140.	1.9	17
143	Osteoporosis imaging: effects of bone preservation on MDCT-based trabecular bone microstructure parameters and finite element models. BMC Medical Imaging, 2015, 15, 22.	1.4	17
144	ADC Quantification of the Vertebral Bone Marrow Water Component: Removing the Confounding Effect of Residual Fat. Magnetic Resonance in Medicine, 2017, 78, 1432-1441.	1.9	17

#	Article	IF	CITATIONS
145	A novel imaging technique for better detecting new lesions in multiple sclerosis. Journal of Neurology, 2017, 264, 1909-1918.	1.8	17
146	Risk of vertebral compression fractures in multiple myeloma patients. Medicine (United States), 2017, 96, e5825.	0.4	17
147	<i>T</i> ₂ mapping with magnetizationâ€prepared 3D TSE based on a modified BIRâ€4Â <i>T</i> ₂ preparation. NMR in Biomedicine, 2017, 30, e3773.	1.6	17
148	Consistency of normalized cerebral blood volume values in glioblastoma using different leakage correction algorithms on dynamic susceptibility contrast magnetic resonance imaging data without and with preload. Journal of Neuroradiology, 2019, 46, 44-51.	0.6	17
149	T2-relaxation time of cartilage repair tissue is associated with bone remodeling after spongiosa-augmented matrix-associated autologous chondrocyte implantation. Osteoarthritis and Cartilage, 2019, 27, 90-98.	0.6	17
150	Balloon osteoplasty—a new technique for minimally invasive reduction and stabilisation of Hill–Sachs lesions of the humeral head: a cadaver study. International Orthopaedics, 2012, 36, 2287-91.	0.9	16
151	Imaging of the lumbar plexus: Optimized refocusing flip angle train design for 3D TSE. Journal of Magnetic Resonance Imaging, 2016, 43, 789-799.	1.9	16
152	FLAIR signal increase of the fluid within the resection cavity after glioma surgery: generally valid as early recurrence marker?. Journal of Neurosurgery, 2017, 127, 417-425.	0.9	16
153	Orthogonally combined motion―and diffusionâ€sensitized driven equilibrium (OCâ€MDSDE) preparation for vessel signal suppression in 3D turbo spin echo imaging of peripheral nerves in the extremities. Magnetic Resonance in Medicine, 2018, 79, 407-415.	1.9	16
154	Acute infarction after mechanical thrombectomy is better delineable in virtual non-contrast compared to conventional images using a dual-layer spectral CT. Scientific Reports, 2018, 8, 9329.	1.6	16
155	Can Early Postoperative O-(2-18FFluoroethyl)-l-Tyrosine Positron Emission Tomography After Resection of Glioblastoma Predict the Location of Later Tumor Recurrence?. World Neurosurgery, 2019, 121, e467-e474.	0.7	16
156	Opportunistic QCT Bone Mineral Density Measurements Predicting Osteoporotic Fractures: A Use Case in a Prospective Clinical Cohort. Frontiers in Endocrinology, 2020, 11, 586352.	1.5	16
157	Al for Doctors—A Course to Educate Medical Professionals in Artificial Intelligence for Medical Imaging. Healthcare (Switzerland), 2021, 9, 1278.	1.0	16
158	Bi-allelic truncating mutations in <i>VWA1</i> cause neuromyopathy. Brain, 2021, 144, 574-583.	3.7	16
159	Progressive disease in glioblastoma: Benefits and limitations of semi-automated volumetry. PLoS ONE, 2017, 12, e0173112.	1.1	16
160	Automated Opportunistic Osteoporosis Screening in Routine Computed Tomography of the Spine: Comparison With Dedicated Quantitative CT. Journal of Bone and Mineral Research, 2020, 37, 1287-1296.	3.1	16
161	Reproducibility of Trabecular Bone Structure Measurements of the Distal Radius at 1.5 and 3.0 T Magnetic Resonance Imaging. Journal of Computer Assisted Tomography, 2012, 36, 623-626.	0.5	15
162	Closed-Cell Stent-Assisted Coiling of Intracranial Aneurysms: Evaluation of Changes in Vascular Geometry Using Digital Subtraction Angiography. PLoS ONE, 2016, 11, e0153403.	1.1	15

#	Article	IF	CITATIONS
163	High Isotropic Resolution T2 Mapping of the Lumbosacral Plexus with T2-Prepared 3D Turbo Spin Echo. Clinical Neuroradiology, 2019, 29, 223-230.	1.0	15
164	Opportunistic osteoporosis screening: contrast-enhanced dual-layer spectral CT provides accurate measurements of vertebral bone mineral density. European Radiology, 2021, 31, 3147-3155.	2.3	15
165	Grading Loss: A Fracture Grade-Based Metric Loss for Vertebral Fracture Detection. Lecture Notes in Computer Science, 2020, , 733-742.	1.0	15
166	3.0 T MR imaging of the ankle: Axial traction for morphological cartilage evaluation, quantitative T2 mapping and cartilage diffusion imaging—A preliminary study. European Journal of Radiology, 2015, 84, 1546-1554.	1.2	14
167	Imaging of the degenerative spine using a sagittal T2-weighted DIXON turbo spin-echo sequence. European Journal of Radiology, 2020, 131, 109204.	1.2	14
168	Vertebral Bone Marrow Heterogeneity Using Texture Analysis of Chemical Shift Encoding-Based MRI: Variations in Age, Sex, and Anatomical Location. Frontiers in Endocrinology, 2020, 11, 555931.	1.5	14
169	X-ray Dark-Field Vector Radiography—A Novel Technique for Osteoporosis Imaging. Journal of Computer Assisted Tomography, 2015, 39, 286-289.	0.5	13
170	Value of Early Postoperative FLAIR Volume Dynamic in Glioma with No or Minimal Enhancement. World Neurosurgery, 2016, 91, 548-559.e1.	0.7	13
171	Influence of Contrast Media on Bone Mineral Density (BMD) Measurements from Routine Contrast-Enhanced MDCT Datasets using a Phantom-less BMD Measurement Tool. RoFo Fortschritte Auf Dem Gebiet Der Rontgenstrahlen Und Der Bildgebenden Verfahren, 2017, 189, 537-543.	0.7	13
172	Isotropic resolution diffusion tensor imaging of lumbosacral and sciatic nerves using a phaseâ€corrected diffusionâ€prepared 3D turbo spin echo. Magnetic Resonance in Medicine, 2018, 80, 609-618.	1.9	13
173	NEWTONIAN AND NON-NEWTONIAN BLOOD FLOW AT A 90â ^{~~} -BIFURCATION OF THE CEREBRAL ARTERY: A COMPARATIVE STUDY OF FLUID VISCOSITY MODELS. Journal of Mechanics in Medicine and Biology, 2018, 18, 1850043.	0.3	13
174	Water T 2 Mapping in Fatty Infiltrated Thigh Muscles of Patients With Neuromuscular Diseases Using a T 2 â€Prepared 3D Turbo Spin Echo With SPAIR. Journal of Magnetic Resonance Imaging, 2020, 51, 1727-1736.	1.9	13
175	Assessment of paraspinal muscle characteristics, lumbar BMD, and their associations in routine multi-detector CT of patients with and without osteoporotic vertebral fractures. European Journal of Radiology, 2020, 125, 108867.	1.2	13
176	T2-Weighted Dixon Turbo Spin Echo for Accelerated Simultaneous Grading of Whole-Body Skeletal Muscle Fat Infiltration and Edema in Patients With Neuromuscular Diseases. Journal of Computer Assisted Tomography, 2018, 42, 574-579.	0.5	12
177	Association of smoking but not HLA-DRB1*15:01, <i>APOE</i> or body mass index with brain atrophy in early multiple sclerosis. Multiple Sclerosis Journal, 2019, 25, 661-668.	1.4	12
178	Effect of MRI acquisition acceleration via compressed sensing and parallel imaging on brain volumetry. Magnetic Resonance Materials in Physics, Biology, and Medicine, 2021, 34, 487-497.	1.1	12
179	Micro-CT vs. Whole Body Multirow Detector CT for Analysing Bone Regeneration in an Animal Model. PLoS ONE, 2016, 11, e0166540.	1.1	12
180	Proposed diagnostic volumetric bone mineral density thresholds for osteoporosis and osteopenia at the cervicothoracic spine in correlation to the lumbar spine. European Radiology, 2022, 32, 6207-6214.	2.3	12

#	Article	IF	CITATIONS
181	Effects of virtual tube current reduction and sparse sampling on MDCT-based femoral BMD measurements. Osteoporosis International, 2018, 29, 2685-2692.	1.3	11
182	MDCT-based Finite Element Analysis of Vertebral Fracture Risk: What Dose is Needed?. Clinical Neuroradiology, 2019, 29, 645-651.	1.0	11
183	Low-dose and sparse sampling MDCT-based femoral bone strength prediction using finite element analysis. Archives of Osteoporosis, 2020, 15, 17.	1.0	11
184	Novel Ultrafast Spiral Head MR Angiography Compared to Standard MR and CT Angiography. Journal of Neuroimaging, 2021, 31, 45-56.	1.0	11
185	Predicting Vertebral Bone Strength Using Finite Element Analysis for Opportunistic Osteoporosis Screening in Routine Multidetector Computed Tomography Scans—A Feasibility Study. Frontiers in Endocrinology, 2020, 11, 526332.	1.5	11
186	Automated detection of the contrast phase in MDCT by an artificial neural network improves the accuracy of opportunistic bone mineral density measurements. European Radiology, 2022, 32, 1465-1474.	2.3	11
187	Multiple sclerosis lesions and atrophy in the spinal cord: Distribution across vertebral levels and correlation with disability. NeuroImage: Clinical, 2022, 34, 103006.	1.4	11
188	Impact of Specific Training in Detecting Osteoporotic Vertebral Fractures on Routine Chest Radiographs. RoFo Fortschritte Auf Dem Gebiet Der Rontgenstrahlen Und Der Bildgebenden Verfahren, 2013, 185, 1074-1080.	0.7	10
189	Correlation of X-Ray Dark-Field Radiography to Mechanical Sample Properties. Microscopy and Microanalysis, 2014, 20, 1528-1533.	0.2	10
190	Evaluation of intra-aneurysmal hemodynamics after flow diverter placement in a patient-specific aneurysm model. Biorheology, 2015, 51, 341-354.	1.2	10
191	Prediction of Vertebral Failure Load by Using X-Ray Vector Radiographic Imaging. Radiology, 2015, 275, 553-561.	3.6	10
192	Pre- and Postcontrast 3D Double Inversion Recovery Sequence in Multiple Sclerosis: A Simple and Effective MR Imaging Protocol. American Journal of Neuroradiology, 2017, 38, 1941-1945.	1.2	10
193	Lumbar muscle and vertebral bodies segmentation of chemical shift encoding-based water-fat MRI: the reference database MyoSegmenTUM spine. BMC Musculoskeletal Disorders, 2019, 20, 152.	0.8	10
194	T2 mapping of the distal sciatic nerve in healthy subjects and patients suffering from lumbar disc herniation with nerve compression. Magnetic Resonance Materials in Physics, Biology, and Medicine, 2020, 33, 713-724.	1.1	10
195	AIFNet: Automatic vascular function estimation for perfusion analysis using deep learning. Medical Image Analysis, 2021, 74, 102211.	7.0	10
196	Scaling relations between trabecular bone volume fraction and microstructure at different skeletal sites. Bone, 2013, 57, 377-383.	1.4	9
197	Effect of radiation dose reduction on texture measures of trabecular bone microstructure: an in vitro study. Journal of Bone and Mineral Metabolism, 2018, 36, 323-335.	1.3	9
198	C1–C2 posterior screw fixation in atlantoaxial fractures revisited: technical update based on 127 cases. European Spine Journal, 2020, 29, 1036-1042.	1.0	9

#	Article	IF	CITATIONS
199	Quantitative Muscle MRI in Patients with Neuromuscular Diseases—Association of Muscle Proton Density Fat Fraction with Semi-Quantitative Grading of Fatty Infiltration and Muscle Strength at the Thigh Region. Diagnostics, 2021, 11, 1056.	1.3	9
200	Prediction of Incidental Osteoporotic Fractures at Vertebral-Specific Level Using 3D Non-Linear Finite Element Parameters Derived from Routine Abdominal MDCT. Diagnostics, 2021, 11, 208.	1.3	9
201	Epidemiology and reporting of osteoporotic vertebral fractures in patients with long-term hospital records based on routine clinical CT imaging. Osteoporosis International, 2022, 33, 685-694.	1.3	9
202	Effect of Low-Dose MDCT and Iterative Reconstruction on Trabecular Bone Microstructure Assessment. PLoS ONE, 2016, 11, e0159903.	1.1	8
203	Computed Tomography and Magnetic Resonance Imaging Parameters Associated with Poor Clinical Outcome in Spondylodiscitis. World Neurosurgery, 2017, 104, 919-926.e2.	0.7	8
204	Geostatistical Analysis of White Matter Lesions in Multiple Sclerosis Identifies Gender Differences in Lesion Evolution. Frontiers in Molecular Neuroscience, 2018, 11, 460.	1.4	8
205	Prognostic value of white matter lesion shrinking in early multiple sclerosis: An intuitive or naÃ ⁻ ve notion?. Brain and Behavior, 2019, 9, e01417.	1.0	8
206	Diffusion tensor imaging and tractography for preoperative assessment of benign peripheral nerve sheath tumors. European Journal of Radiology, 2020, 129, 109110.	1.2	8
207	Age- and BMI-related variations of fat distribution in sacral and lumbar bone marrow and their association with local muscle fat content. Scientific Reports, 2020, 10, 9686.	1.6	8
208	Age- and gender-related variations of cervical muscle composition using chemical shift encoding-based water-fat MRI. European Journal of Radiology, 2020, 125, 108904.	1.2	8
209	A short history of thrombectomy – Procedure and success analysis of different endovascular stroke treatment techniques. Interventional Neuroradiology, 2021, 27, 249-256.	0.7	8
210	MRÂimaging by 3D T1-weighted black blood sequences may improve delineation of therapy-naive high-grade gliomas. European Radiology, 2021, 31, 2312-2320.	2.3	8
211	Texture Features of Proton Density Fat Fraction Maps from Chemical Shift Encoding-Based MRI Predict Paraspinal Muscle Strength. Diagnostics, 2021, 11, 239.	1.3	8
212	Texture Analysis Using CT and Chemical Shift Encoding-Based Water-Fat MRI Can Improve Differentiation Between Patients With and Without Osteoporotic Vertebral Fractures. Frontiers in Endocrinology, 2021, 12, 778537.	1.5	8
213	Accuracy and Reproducibility of Adipose Tissue Measurements in Young Infants by Whole Body Magnetic Resonance Imaging. PLoS ONE, 2015, 10, e0117127.	1.1	7
214	A Radiomics Approach to Traumatic Brain Injury Prediction in CT Scans. , 2019, , .		7
215	Differentiation of Acute/Subacute versus Old Vertebral Fractures in Multislice Detector Computed Tomography: Is Magnetic Resonance Imaging Always Needed?. World Neurosurgery, 2019, 122, e676-e683.	0.7	7
216	Finite Element Analysis-Based Vertebral Bone Strength Prediction Using MDCT Data: How Low Can We Go?. Frontiers in Endocrinology, 2020, 11, 442.	1.5	7

#	Article	IF	CITATIONS
217	Subtraction Maps Derived from Longitudinal Magnetic Resonance Imaging in Patients with Glioma Facilitate Early Detection of Tumor Progression. Cancers, 2020, 12, 3111.	1.7	7
218	Regional variation of thigh muscle fat infiltration in patients with neuromuscular diseases compared to healthy controls. Quantitative Imaging in Medicine and Surgery, 2021, 11, 2610-2621.	1.1	7
219	Gender-, Age- and Region-Specific Characterization of Vertebral Bone Microstructure Through Automated Segmentation and 3D Texture Analysis of Routine Abdominal CT. Frontiers in Endocrinology, 2021, 12, 792760.	1.5	7
220	The 3D-based scaling index algorithm to optimize structure analysis of trabecular bone in postmenopausal women with and without osteoporotic spine fractures. , 2004, , .		6
221	Early Changes of Trabecular Bone Structure in Asymptomatic Subjects With Knee Malalignment. Journal of Computer Assisted Tomography, 2014, 38, 137-141.	0.5	6
222	Fractional Anisotropy Correlates with Overall Survival in Glioblastoma. World Neurosurgery, 2016, 95, 525-534.e1.	0.7	6
223	Uncertainty quantification in brain tumor segmentation using CRFs and random perturbation models. , 2016, , .		6
224	Effect of Statistically Iterative Image Reconstruction on Vertebral Bone Strength Prediction Using Bone Mineral Density and Finite Element Modeling. Journal of Computer Assisted Tomography, 2019, 43, 61-65.	0.5	6
225	Systematic Evaluation of Low-dose MDCT for Planning Purposes of Lumbosacral Periradicular Infiltrations. Clinical Neuroradiology, 2020, 30, 749-759.	1.0	6
226	Super-selective ASL and 4D ASL-based MR Angiography in aÂPatient with Moyamoya Disease. Clinical Neuroradiology, 2021, 31, 515-519.	1.0	6
227	Assessment of the Extent of Resection in Surgery of High-Grade Glioma—Evaluation of Black Blood Sequences for Intraoperative Magnetic Resonance Imaging at 3 Tesla. Cancers, 2020, 12, 1580.	1.7	6
228	Low-dose MDCT: evaluation of the impact of systematic tube current reduction and sparse sampling on the detection of degenerative spine diseases. European Radiology, 2021, 31, 2590-2600.	2.3	6
229	Improved Reliability of Automated ASPECTS Evaluation Using Iterative Model Reconstruction from Head CT Scans. Journal of Neuroimaging, 2021, 31, 341-347.	1.0	6
230	Occult Disco-Ligamentous Lesions of the Subaxial c-Spine—A Comparison of Preoperative Imaging Findings and Intraoperative Site Inspection. Diagnostics, 2021, 11, 447.	1.3	6
231	Prediction of incident vertebral fractures in routine MDCT: Comparison of global texture features, 3D finite element parameters and volumetric BMD. European Journal of Radiology, 2021, 141, 109827.	1.2	6
232	Simulation Training in Neuroangiography: Transfer to Reality. CardioVascular and Interventional Radiology, 2020, 43, 1184-1191.	0.9	6
233	Tracking the Corticospinal Tract in Patients With High-Grade Glioma: Clinical Evaluation of Multi-Level Fiber Tracking and Comparison to Conventional Deterministic Approaches. Frontiers in Oncology, 2021, 11, 761169.	1.3	6
234	Multi-scanner and multi-modal lumbar vertebral body and intervertebral disc segmentation database. Scientific Data, 2022, 9, 97.	2.4	6

#	Article	IF	CITATIONS
235	Imaging of the Osteoporotic Spine – Quantitative Approaches in Diagnostics and for the Prediction of the Individual Fracture Risk. RoFo Fortschritte Auf Dem Gebiet Der Rontgenstrahlen Und Der Bildgebenden Verfahren, 2022, 194, 1088-1099.	0.7	6
236	Ganglia of the tarsal sinus: MR imaging features and clinical findings. European Journal of Radiology, 2011, 80, e394-e400.	1.2	5
237	Alignment does not influence cartilage T2 in asymptomatic knee joints. Knee Surgery, Sports Traumatology, Arthroscopy, 2014, 22, 1396-1403.	2.3	5
238	Longitudinal changes in subchondral bone structure as assessed with MRI are associated with functional outcome after high tibial osteotomy. Journal of ISAKOS, 2018, 3, 205-212.	1.1	5
239	MRI criteria of subtypes of adenomas and epithelial cysts of the pituitary gland. Neurosurgical Review, 2020, 43, 265-272.	1.2	5
240	Regional variation in paraspinal muscle composition using chemical shift encoding-based water-fat MRI. Quantitative Imaging in Medicine and Surgery, 2020, 10, 496-507.	1.1	5
241	Association of thigh and paraspinal muscle composition in young adults using chemical shift encoding-based water–fat MRI. Quantitative Imaging in Medicine and Surgery, 2020, 10, 128-136.	1.1	5
242	Spine surgery in pregnant women: a multicenter case series and proposition of treatment algorithm. European Spine Journal, 2021, 30, 809-817.	1.0	5
243	MDCT-Based Finite Element Analyses: Are Measurements at the Lumbar Spine Associated with the Biomechanical Strength of Functional Spinal Units of Incidental Osteoporotic Fractures along the Thoracolumbar Spine?. Diagnostics, 2021, 11, 455.	1.3	5
244	Low-Dose MDCT of Patients With Spinal Instrumentation Using Sparse Sampling: Impact on Metal Artifacts. American Journal of Roentgenology, 2021, 216, 1308-1317.	1.0	5
245	T2 mapping of lumbosacral nerves in patients suffering from unilateral radicular pain due to degenerative disc disease. Journal of Neurosurgery: Spine, 2019, 30, 750-758.	0.9	5
246	Impact of dose reduction and iterative model reconstruction on multi-detector CT imaging of the brain in patients with suspected ischemic stroke. Scientific Reports, 2021, 11, 22271.	1.6	5
247	Characterizing trabecular bone structure for assessing vertebral fracture risk on volumetric quantitative computed tomography. , 2015, 9417, .		4
248	Diagnostic Potential of Pulsed Arterial Spin Labeling in Alzheimer's Disease. Frontiers in Neuroscience, 2016, 10, 154.	1.4	4
249	Computed Tomography Findings Associated with Clinical Outcome After Dynamic Posterior Stabilization of the Lumbar Spine. World Neurosurgery, 2016, 93, 306-314.	0.7	4
250	Correlating subcortical interhemispheric connectivity and cortical hemispheric dominance in brain tumor patients: A repetitive navigated transcranial magnetic stimulation study. Clinical Neurology and Neurosurgery, 2016, 141, 56-64.	0.6	4
251	Predicting brain tumor regrowth in relation to motor areas by functional brain mapping. Neuro-Oncology Practice, 2018, 5, 82-95.	1.0	4
252	CFD and MRI studies of hemodynamic changes after flow diverter implantation in a patient-specific model of the cerebral artery. Experiments in Fluids, 2018, 59, 1.	1.1	4

#	Article	IF	CITATIONS
253	Vertebral bone marrow fat fraction changes in postmenopausal women with breast cancer receiving combined aromatase inhibitor and bisphosphonate therapy. BMC Musculoskeletal Disorders, 2019, 20, 515.	0.8	4
254	Tube Current Reduction in CT Angiography: How Low Can We Go in Imaging of Patients With Suspected Acute Stroke?. American Journal of Roentgenology, 2019, 213, 410-416.	1.0	4
255	Gadolinium-Enhanced 3D T1-Weighted Black-Blood MR Imaging for the Detection of Acute Optic Neuritis. American Journal of Neuroradiology, 2020, 41, 2333-2338.	1.2	4
256	Image Analysis Reveals Microstructural and Volumetric Differences in Glioblastoma Patients with and without Preoperative Seizures. Cancers, 2020, 12, 994.	1.7	4
257	T1-Weighted Intensity Increase After aÂSingle Administration of aÂLinear Gadolinium-Based Contrast Agent in Multiple Sclerosis. Clinical Neuroradiology, 2021, 31, 235-243.	1.0	4
258	Local Bone Mineral Density, Subcutaneous and Visceral Adipose Tissue Measurements in Routine Multi Detector Computed Tomography—Which Parameter Predicts Incident Vertebral Fractures Best?. Diagnostics, 2021, 11, 240.	1.3	4
259	Gray matter atrophy in relapsing-remitting multiple sclerosis is associated with white matter lesions in connecting fibers. Multiple Sclerosis Journal, 2022, 28, 900-909.	1.4	4
260	Robust, Primitive, and Unsupervised Quality Estimation for Segmentation Ensembles. Frontiers in Neuroscience, 2021, 15, 752780.	1.4	4
261	Uncertainty-Aware and Lesion-Specific Image Synthesis in Multiple Sclerosis Magnetic Resonance Imaging: A Multicentric Validation Study. Frontiers in Neuroscience, 2022, 16, 889808.	1.4	4
262	Patient-Specific Finite Element Modeling of the Whole Lumbar Spine Using Clinical Routine Multi-Detector Computed Tomography (MDCT) Data—A Pilot Study. Biomedicines, 2022, 10, 1567.	1.4	4
263	Emerging Research on Bone Health Using High-Resolution CT and MRI. Current Radiology Reports, 2014, 2, 1.	0.4	3
264	Increase in FLAIR Signal of the Fluid Within the Resection Cavity as Early Recurrence Marker: Also Valid for Brain Metastases?. RoFo Fortschritte Auf Dem Gebiet Der Rontgenstrahlen Und Der Bildgebenden Verfahren, 2016, 189, 63-70.	0.7	3
265	Implementation of a sagittal T2-weighted DIXON turbo spin-echo sequence may shorten MRI acquisitions in the emergency setting of suspected spinal bleeding. European Radiology Experimental, 2021, 5, 19.	1.7	3
266	Multi-detector computed tomography (MDCT) imaging: association of bone texture parameters with finite element analysis (FEA)-based failure load of single vertebrae and functional spinal units. Quantitative Imaging in Medicine and Surgery, 2021, 11, 2955-2967.	1.1	3
267	Association of Cervical and Lumbar Paraspinal Muscle Composition Using Texture Analysis of MR-Based Proton Density Fat Fraction Maps. Diagnostics, 2021, 11, 1929.	1.3	3
268	Low-dose multi-detector computed tomography for periradicular infiltrations at the cervical and lumbar spine. Scientific Reports, 2022, 12, 4324.	1.6	3
269	Reply to letter to the editor: "Is balloon osteoplasty attractive or questionable treatment for Hill-Sachs lesions?― International Orthopaedics, 2012, 36, 2599-2600.	0.9	2
270	Automated segmentation reveals silent radiographic progression in adult-onset vanishing white-matter disease. Neuroradiology Journal, 2017, 30, 5-9.	0.6	2

#	Article	IF	CITATIONS
271	Wavelet-based reconstruction of dynamic susceptibility MR-perfusion: a new method to visualize hypervascular brain tumors. European Radiology, 2019, 29, 2669-2676.	2.3	2
272	Magnetic resonance neurography of the lumbosacral plexus at 3 Tesla – CSF-suppressed imaging with submillimeter resolution by a three-dimensional turbo spin echo sequence. Magnetic Resonance Imaging, 2020, 71, 132-139.	1.0	2
273	Association of Thigh Muscle Strength with Texture Features Based on Proton Density Fat Fraction Maps Derived from Chemical Shift Encoding-Based Water–Fat MRI. Diagnostics, 2021, 11, 302.	1.3	2
274	MDCT-Based Finite Element Analysis for the Prediction of Functional Spine Unit Strength—An In Vitro Study. Materials, 2021, 14, 5791.	1.3	2
275	Anatomy-Aware Inference of the 3D Standing Spine Posture from 2D Radiographs. Tomography, 2022, 8, 479-496.	0.8	2
276	Finite Element Analysis of Osteoporotic and Osteoblastic Vertebrae and Its Association With the Proton Density Fat Fraction From Chemical Shift Encoding-Based Water-Fat MRI – A Preliminary Study. Frontiers in Endocrinology, 0, 13, .	1.5	2
277	Clinical Pilot Study for the Automatic Segmentation and Recognition of Abdominal Adipose Tissue Compartments from MRI Data. RoFo Fortschritte Auf Dem Gebiet Der Rontgenstrahlen Und Der Bildgebenden Verfahren, 2012, 184, 548-555.	0.7	1
278	Predicting the biomechanical strength of proximal femur specimens with bone mineral density features and support vector regression. Proceedings of SPIE, 2012, , .	0.8	1
279	Change assessment for CT spine imaging. , 2013, , .		1
280	Predicting the biomechanical strength of proximal femur specimens with Minkowski functionals and support vector regression. , 2014, 9038, .		1
281	Use of MR-based trabecular bone microstructure analysis at the distal radius for osteoporosis diagnostics: a study in post-menopausal women with breast cancer and treated with aromatase inhibitor. Clinical Cases in Mineral and Bone Metabolism, 2016, 13, 29-32.	1.0	1
282	Computer assisted evaluation of plate osteosynthesis of diaphyseal femur fracture considering interfragmentary movement: a finite element study. Biomedizinische Technik, 2017, 62, 245-255.	0.9	1
283	CSF Protein Concentration Shows No Correlation With Brain Volume Measures. Frontiers in Neurology, 2019, 10, 463.	1.1	1
284	Structured Reporting of Acute Ischemic Stroke – Consensus-Based Reporting Templates for Non-Contrast Cranial Computed Tomography, CT Angiography, and CT Perfusion. RoFo Fortschritte Auf Dem Gebiet Der Rontgenstrahlen Und Der Bildgebenden Verfahren, 2021, 193, 1315-1317.	0.7	1
285	High-Resolution Imaging. Medical Radiology, 2013, , 149-159.	0.0	0
286	Predicting the biomechanical strength of proximal femur specimens through high dimensional geometric features and support vector regression. , 2013, 8672, .		0
287	MR-based trabecular bone microstructure is not altered in subjects with indolent systemic mastocytosis. Clinical Imaging, 2015, 39, 886-889.	0.8	0
288	Effect of low-dose CT and iterative reconstruction on trabecular bone microstructure assessment. Proceedings of SPIE, 2016, , .	0.8	0

#	Article	IF	CITATIONS
289	Assessing vertebral fracture risk on volumetric quantitative computed tomography by geometric characterization of trabecular bone structure. Proceedings of SPIE, 2016, 9785, .	0.8	Ο
290	Effects of sparse sampling in combination with iterative reconstruction on quantitative bone microstructure assessment. , 2017, , .		0
291	Pre-contrast T1-weighted imaging of the spinal cord may be unnecessary in patients with multiple sclerosis. European Radiology, 2021, 31, 9316-9323.	2.3	Ο
292	Low-dose MDCT: evaluation of the impact of systematic tube current reduction and sparse sampling on quantitative paraspinal muscle assessment. Quantitative Imaging in Medicine and Surgery, 2021, 11, 3042-3050.	1.1	0
293	Low-Dose Simulation and Sparse Sampling with Statistical Iterative Reconstruction: Dose Reduction in MDCT-Based Bone Mineral Density and Microstructure Assessment. Seminars in Musculoskeletal Radiology, 2017, 21, S1-S5.	0.4	0
294	Calcium decomposition and phantomless bone mineral density measurements using dual-layer-based spectral computed tomography. , 2018, , .		0
295	Association of quadriceps muscle, gluteal muscle, and femoral bone marrow composition using chemical shift encoding-based water-fat MRI: a preliminary study in healthy young volunteers. European Radiology Experimental, 2020, 4, 35.	1.7	0